# Synthesis of large-area rhombohedral few-layer graphene by chemical vapor deposition on copper

Chamseddine Bouhafs [a, b, **], Sergio Pezzini [a, b, c], Fabian R. Geisenhof [d], Neeraj Mishra [a, b], Vaidotas Mišeikis [a, b], Yuran Niu [e], Claudia Struzzi [e], R. Thomas Weitz [d, f, g], Alexei A. Zakharov [e], Stiven Forti [a], Camilla Coletti [a, b, *]

[a] Center for Nanotechnology Innovation @ NEST, Istituto Italiano di Tecnologia, Piazza San Silvestro 12, 56127, Pisa, Italy
[b] Graphene Labs, Istituto Italiano di Tecnologia, Via Morego 30, 16163, Genova, Italy
[c] NEST, Istituto Nanoscienze-CNR and Scuola Normale Superiore, Piazza San Silvestro 12, 56127, Pisa, Italy
[d] Physics of Nanosystems, Department of Physics, Ludwig-Maximilians-University Munich, Geschwister-Scholl-Platz 1, 80799, Munich, Germany
[e] MAX IV Laboratory, University of Lund, 22100, Lund, Sweden
[f] Center for Nanoscience (CeNS), Schellingstrasse 4, 80799, Munich, Germany
[g] I. Physical Institute, Faculty of Physics, Georg-August-University Göttingen, Friedrich-Hund-Platz 1, 37077, Göttingen, Germany

## ARTICLE INFO

## ABSTRACT

Rhombohedral-stacked few-layer graphene (FLG) displays peculiar electronic properties that could lead to phenomena such as high-temperature superconductivity and magnetic ordering. To date, experimental studies have been mainly limited by the difficulty in isolating rhombohedral FLG with thickness exceeding 3 layers and device-compatible size. In this work, we demonstrate the synthesis and transfer of rhombohedral graphene with thickness up to 9 layers and areas up to ~50 μm². The domains of rhombohedral FLG are identified by Raman spectroscopy and are found to alternate with Bernal regions within the same crystal in a stripe-like configuration. Near-field nano-imaging further confirms the structural integrity of the respective stacking orders. Combined spectroscopic and microscopic analyses indicate that rhombohedral-stacking formation is strongly correlated to the underlying copper step-bunching and emerges as a consequence of interlayer displacement along preferential crystallographic orientations. The growth and transfer of rhombohedral FLG with the reported thickness and size shall facilitate the observation of predicted unconventional physics and ultimately add to its technological relevance.

## 1. Introduction

The number of atomic layers and the interlayer stacking order determine the physical properties of van der Waals materials (vdWm) [1]. Few-layer graphene (FLG) is a naturally occurring vdWm, comprising graphene sheets in number $N_G \geq 3$, with two stable configurations, characterized by either Bernal (ABA) [2] or rhombohedral (ABC) stacking [3]. In ABA stacking, within the $N_G = 3$ minimal constituents, the positions of the atoms of the topmost layer exactly match those of the bottom layer. While for ABC stacking, each layer is laterally shifted with respect to the layer below by an interatomic spacing distance. Concerning the electronic properties, ABA-FLG is a semi-metal with overlapping bands [4,5]. In contrast, ABC-FLG possesses a tunable bandgap [6–8] and surface states with increasingly "flat" band dispersion for increasing $N_G$ [9–13]. Due to the large density of states and reduced kinetic energy within the flat band, ABC-FLG is susceptible to strong electronic correlation, which makes it a model system for investigating high-temperature superconductivity [11,14,15] and magnetism [16–19], as well as for realizing novel electronic applications [20].

The main factor constraining the flourishing of ABC-FLG in such research fields is the lack of a synthesis and/or transfer techniques that can yield high-quality large-area FLG with controllable properties ($N_G$ and stacking order) on insulating substrates. Micro-

mechanical exfoliation can produce pristine ABC-FLG domains with different thicknesses ($N_G$ from 3 up to 27) and relatively large lateral size (up to few tens of micrometers) [13,18,21]. Kish graphite, as the material source for exfoliation, contains typically 80% ABA, 14% ABC, and 6% turbostratic structure [3,22]. As a result, the exfoliation technique suffers from a limited yield of ABC-FLG. Although suitable for fundamental studies, this method is not scalable and the control over $N_G$ remains approximate and not reproducible. ABC-FLG with high crystal quality has been synthesized using thermal decomposition (i.e. sublimation) of silicon carbide (SiC), both on 3C−SiC(111) [12,23,24] and 6H−SiC(0001) [25]. However, the domains with uniform thickness presently remain limited to a few hundred nanometers [24,25] and it is generally not sufficient for device fabrication.

Furthermore, ABC-FLG is subjected to phase transformation to ABA under external stimuli, such as shear stress [26,27], joule heating and laser illumination [28] or field-effect doping [29]. Therefore, alternative methods to produce ABC-FLG over large scale need to be combined with low-impact transfer and handling approaches capable of preserving the rhombohedral stacking.

Chemical vapor deposition (CVD) is considered a viable route to synthesize high-quality large-area single-crystal monolayer (1L) graphene on copper (Cu) substrates [30−33]. However, the growth of large-area FLG with controlled $N_G$ and stacking using CVD on Cu is challenging, primarily due to a self-limiting mechanism after the formation of 1L [34]. Recent progress in CVD growth showed the possibility to controllably synthesize large-area bilayer (2L) and trilayer (3L) graphene with different stackings. For example, large AB-stacked 2L graphene (100−500 μm$^2$) was grown on Cu foils using the so-called pocket growth technique [31]. Centimeter-scale ABA-stacked 3L graphene films were obtained by CVD on single-crystal Cu/Ni(111) alloy [35]. Nevertheless, ABC-3L graphene remains limited to a few micrometers wide domains when synthesized on Cu [36] or Cu/Ni substrates [37]. Taming CVD growth to obtain high-quality large-area of ABC-FLG with $N_G > 3$ would allow further understanding of the physical properties of ABC-FLG and its integration in novel device concepts.

In this work, we use low-pressure chemical vapor deposition (LPCVD) to grow FLG crystals on Cu substrate. By optimizing our growth conditions, we obtain large-area FLG with varying $N_G$ (up to 9L). The transfer of FLG onto SiO$_2$ substrates is carried out via etch-free delamination. Subsequent Raman investigations show that the FLG crystals are composed of alternating domains with ABA and ABC stacking. The domains of ABC-FLG have a large size (up to 4 μm width and 90 μm long), which is a significant improvement with respect to what is reported in literature (see Table 1 in supplementary material). Using infrared nano-imaging, we can resolve the domains on the nanoscale, confirming that the stripes are single crystals of alternating stacking order. Combined experimental observations reveal how the Cu surface morphology controls the occurrence of the ABC-FLG stripes.

## 2. Experimental

### 2.1. Growth of FLG on Cu

FLG crystals are grown by using a 4-inch Aixtron BM-Pro cold-wall (CW) CVD reactor. CW CVD reactors have several advantages for the cost-effective growth of high-quality graphene such as rapid sample heating and cooling times and fast growth rates [38], as well as cleanness and limitation of inorganic contaminations [39,40]. An electropolished 25 μm Cu foil (Alfa-Aesar #46365, 99.8% purity) is used as a substrate and the effective gas flow is reduced by a sample enclosure. A targeted copper foil layout is specifically devised for this growth process as shown in Fig. 1(a−c) and explained in detail

in the Results and Discussion section. The growth process is similar to the one used by Mišeikis et al. [30] and it consists of four steps. With respect to Ref. [30], growth conditions are optimized to achieve large-area of FLG. The temperature of the furnace is increased up to an optimized value ($T_G$ = 1070 °C, calibrated according to the melting point of Cu) in Ar atmosphere (temperature ramp-up step), then it is maintained constant for 10 min (annealing step). The sample enclosure and annealing step serve to reduce the density of nucleation centers [30]. For the growth step, CH$_4$ and H$_2$ (99.9999% purity) are used as carbon source and as a catalyst in formation of active surface-bound carbon, respectively. Ar is used as a carrier gas. The flow rates are set to 90 sccm, 0.7 sccm and 900 sccm, for H$_2$, CH$_4$ and Ar, respectively. The temperature during growth is kept to $T_G \pm 1$ °C for 90 min. The annealing and growth temperature of 1070 °C allows increasing the size of Cu domains and of graphene crystals, respectively, without the risk of melting the Cu substrate (Cu melting point ~1084 °C). Finally, the chamber is cooled down in Ar atmosphere (cool-down step). During the whole process, the pressure is maintained at ~25 mbar.

### 2.2. FLG transfer to SiO$_2$/Si and ZLG/SiC substrate

The as-grown FLG crystals on Cu are transferred to either SiO$_2$/Si or buffer layer/6H−SiC(0001) substrates (ZLG/SiC) by a semi-dry transfer (etch-free delamination) [41−43]. We adopt throughout the text the term ZLG to indicate the first carbon-rich layer that develops on top of SiC(0001): in this layer the carbon atoms are disposed in a graphene like hexagonal lattice but 30% of them are covalently bounded to the Si atoms of the SiC substrate and for this reason ZLG does not present graphene electronic properties [44]. We use a spin-coated soft polymeric membrane and a semi-rigid PDMS frame to support the crystals during electrochemical delamination in 0.1 M NaOH aqueous solution. The Cu foil is connected to a DC voltage generator and set to 2.4 V with respect to a Pt counter-electrode, during 10−15 min. After detachment, the polymer-supported crystals are released on the final substrate heated at 90 °C, the PDMS is peeled off and the membrane is cleaned in organic solvents overnight. These transfer techniques preserve the Cu substrate after the graphene detachment and as result, the surface morphology of the leftover Cu substrate can be investigated.

### 2.3. Characterization

The layer thickness and the stacking order of the FLG crystals on SiO$_2$/Si substrate are determined via micro-Raman scattering spectroscopy. Raman measurements are performed in backscattering geometry under ambient conditions, using a Renishaw InVia spectrometer (1800 grooves/mm) equipped with a Peltier-cooled CCD detector with spectral resolution ~2 cm$^{-1}$. The samples are excited with the 532 nm (2.33 eV) line of a diode-pumped frequency-doubled solid-state Nd: YAG laser through 100 × objective (NA 0.9). The laser spot diameter and power are ~1 μm and ~1 mW, respectively. To perform Raman mappings, we used a motorized XYZ stage, with a step size of 0.5 or 1 μm.

The infrared nano-imaging was performed using a commercial scattering-type scanning near-field microscope (s-SNOM, neaspec GmbH). Focusing an infrared CO$_2$ laser beam with a wavelength of about 10.5 μm onto a metal coated atomic force microscopy tip (Pt/Ir, Arrrow NCPT-50, Nanoworld), while operating the system in tapping mode provides topography and infrared nano-images of the graphene samples simultaneously. The oscillation frequency and amplitude of the tip were about 250−270 kHz and 50−80 nm, respectively. The AFM tip transforms the incident infrared beam into a highly confined and enhanced electromagnetic field. This
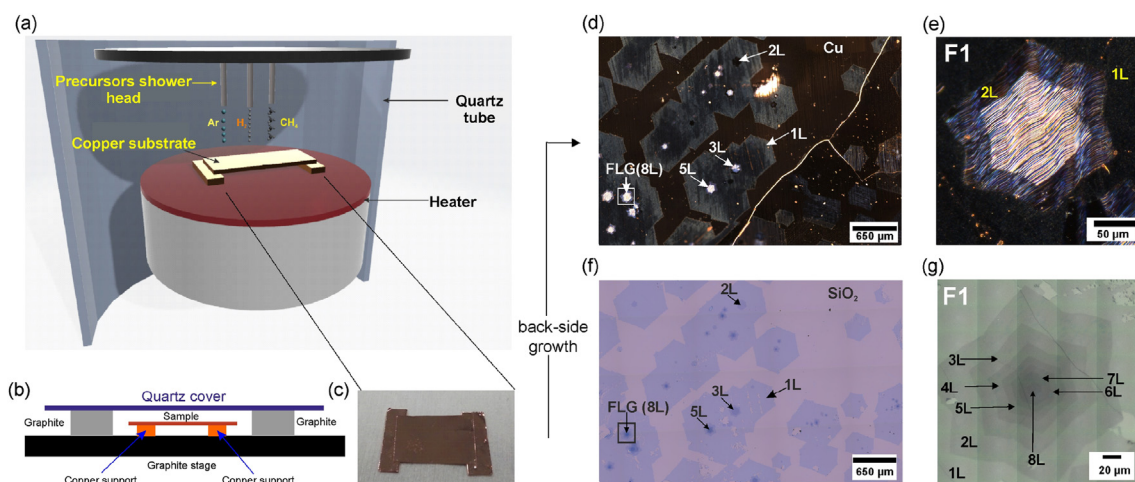
**Fig. 1.** a) Schematics of the CVD setup for FLG crystals growth. b) Cross-sectional sketch of the optimized growth layout. c) BF-OM of a Cu foil suspended over Cu supports, after FLG growth. d) DF-OM image of a representative as-grown FLG/Cu sample. e) Zoom-in on FLG crystal F1 (white square in d)). f) BF-OM image of the same FLG sample after transfer to SiO₂/Si. g) BF-OM of FLG F1 after transfer (black square in f)). (A colour version of this figure can be viewed online.)

nanofocus enables a near-field interaction with the graphene sample underneath, while its magnitude depends on the local dielectric properties/optical conductivity of graphene and is therefore sensitive to layer number, stacking order and twist angle [27,45,46]. The near-field information is extracted from the back-scattered light, which is detected by a HgCdTe detector. The signal in all near-field nano-images shown is lock-in filtered at the fourth harmonic frequency of the tip's oscillation to avoid any far-field background.

The surface morphologies of the FLG samples and Cu foils are characterized using bright-field (BF) and dark-field (DF) optical microscopy (OM), and tapping mode atomic force microscopy (AFM). The OM and AFM images are acquired using a Leica DM8000 M light microscope (equipped with a DF condenser) and Bruker Dimension Icon, respectively. The morphology of Cu substrates after the graphene transfer is investigated using scanning electron microscopy (SEM). The SEM images are acquired using Zeiss Merlin with an accelerating voltage of 5 kV.

Low-energy electron microscopy (LEEM) and low-energy electron diffraction (LEED) are performed in ultrahigh vacuum and carried out using a spectroscopic photoemission and low energy electron microscope (SPELEEM) instrument at MAXPEEM beamline in the MAX IV Laboratory, Lund, Sweden. Measurements in SPE-LEEM require conductive and flat substrates. To satisfy these conditions, we have used FLG crystals transferred on ZLG on semiconductive SiC. The ZLG substrates are prepared via SiC sublimation under Ar atmosphere [47].

## 3. Results and discussion

As shown in Fig. 1(a−c), we developed a new layout for the growth on Cu foil. This configuration combines the advantages of the back-side diffusion process of Cu pockets [31] with the ability to keep a flat growth template (see Fig. 1(c)), which facilitates the subsequent transfer. The Cu foil is suspended over two Cu supports (about 100 μm thick) placed on top of the graphite stage. A custom-made quartz enclosure is adopted to achieve more reproducible atmospheric and thermal conditions (by reducing the volume of the "growth zone") and as a physical barrier to reduce the effective gas flow [30]. While the top face of the foil, directly exposed to the gas flow, undergoes full graphitic material coverage, we successfully grew isolated FLG crystals on the bottom side. Fig. 1(d) shows a

typical DF-OM image obtained after growing FLG crystals on the backside of a suspended Cu foil (Fig. 1(c)). Numerous 1L crystals are clearly visible, with a distinctive hexagonal shape and partial merging between adjacent ones.

The typical lateral size of the 1L crystals is 600 μm. FLG areas, positioned at the center of the 1L, are detected as brighter regions with typical 90 μm lateral size. In general, the visibility of the 1L crystals and of the adlayers in DF-OM is different for different Cu grains (see full foil DF-OM in Fig. S1 in supporting information). A zoom-in view of FLG crystal F1 (white rectangle in Fig. 1(d)) is shown in Fig. 1(e). For CVD growth of graphene on Cu, the Cu surface underneath the graphene undergoes step bunching (SB). The step height depends on $N_G$ and it is found that increasing $N_G$ favors higher steps [48−50]. SB with different height scatter the incident light with varying intensities, resulting in different DF-OM response, with higher steps being brighter as reported previously [48]. Both the absence of contrast for the (rather flat) bare Cu outside graphene and the bright blue color for some of the crystals are well understood in the standard description of Rayleigh scattering [48]. In Fig. 1(e) one can appreciate the wave-like Cu steps underneath graphene, as well as their increasing brightness as a function of $N_G$, which permits a conclusive distinction of adlayers up to 3L.

To gain further information about $N_G$ and the orientation of the adlayers in the FLG crystals, the as-grown samples are transferred on SiO₂/Si substrates (Fig. 1(f)) with a semi-dry transfer approach, that allows maintaining the exceptional properties of graphene as recently demonstrated by transport measurements on 1L [51]. We noticed that transferring FLG results in a higher number of tears and breaks (mostly observed on the 1L parts) with respect to transferring 1L or 2L crystals with the same technique. These tears/breaks are likely due to the fact that thick FLG causes a larger amount of stress on the 1L, which acts as a support layer for FLG during detachment from Cu. Nonetheless, the majority of the transferred FLG was intact in the regions with $N_G \geq 3$, which represent an ideal platform for experimental studies. Fig. 1(g) shows a BF-OM image of the same FLG shown in DF-OM in Fig. 1(e) (crystal F1), after semi-dry transfer. On SiO₂/Si, $N_G$ can be straightforwardly identified [52]: up to 8L thickness is observed. From BF-OM after the transfer, we find that the typical lateral domain sizes of the FLG grown with our process are approximately 600 μm, 150 μm, 90 μm, 70 μm, 50 μm, 35 μm, 25 μm, 20 μm and

7 μm for 1L, 2L, 3L, 4L, 5L, 6L, 7L, 8L and 9L, respectively. Additionally, BF-OM allows for a straightforward discerning of the relative interlayer rotation in CVD-grown FLG crystals, which is revealed by the hexagonally-shaped adlayers' orientation. We find that, for our growth conditions, 40% of the FLG crystals present aligned stacking (the inner and outer hexagons have the same orientation), while the remaining 60% show rotated R30 or turbostratic stacking [53]. Such optical assessment was confirmed by Raman analysis, based on the 2D band lineshape and width [54,55] (see Fig. S2 in supporting information).

To check for the presence and properties of ABC-FLG, we carried out a detailed Raman study on FLG crystals, like that reported in Fig. 2(a), that showed in BF-OM aligned stacking (i.e. no interlayer rotation). To date, the Raman signatures of ABA and ABC-stacking in exfoliated FLG have been widely investigated and it has been shown that ABA and ABC-FLG have distinct Raman 2D band lineshapes. The 2D band of ABC-FLG is broader (i.e. larger full-width-at-half-maximum (FWHM) values) with respect to that of ABA-FLG [21,22,56–58]. Also, an additional Raman fingerprint for ABC-FLG is given by the LO + ZO' (~1748 cm$^{-1}$) combination mode of the M band [58,59], where LO and ZO' are in-plane and out-of-plane interlayer breathing optical phonon modes, respectively. Our procedure to identifying ABC-FLG consisted in the following steps:

*(i)* Performing Raman mapping of the 2D band of FLG and fitting each spectrum with a single peak function, as done in previous literature to reliably identify different stacking orders [22,56]. *(ii)* identifying as possible ABC-FLG regions with FWHM(2D) (larger than a thickness-dependent threshold) and the symmetry of the 2D lineshape. *(iii)* conclusively identifying those areas as ABC- FLG by performing M band Raman analysis.

Here, we report the Raman analysis for the 9L crystal reported in Fig. 2(a) (see Fig. S3 in supporting information for $N_G$ determination from the intensity profile and Fig. S4 for Raman mapping of other two crystals, F3 and F4).

Fig. 2(b) shows a color map of FWHM(2D), acquired over the area indicated by the black rectangle in Fig. 2(a). FLG exhibits two distinctive types of domains, with clear difference in FWHM(2D) for fixed $N_G$. The domains form parallel stripes, showing alternating

narrow and broad FWHM(2D), and extending across regions with different $N_G$. Fig. 2(c) shows representative 2D bands for the two types of domains, for 3L, 4L, 5L, 6L and 7L graphene, where the Raman data from the stripes with low and high FWHM(2D) are plotted as blue and red lines, respectively. The lineshape of the blue and red curves are entirely comparable to those reported for exfoliated FLG with ABA and ABC stacking, respectively [22,56,58]. Raman M band of each stripe-domain further confirms our initial assessment. Fig. 2(d) shows the M band region for our 3L, 4L, 5L, 6L and 7L graphene. The LO + ZO' splits into two subpeaks ($P_{21}$ and $P_{22}$) for ABC 3L and 4L. For ABC 5L, 6L and 7L, LO + ZO' splits into three ($P_{21}$, $P_{22}$ and $P_{23}$), four ($P_{21}$, $P_{22}$, $P_{23}$ and $P_{24}$) and five ($P_{21}$, $P_{22}$, $P_{23}$, $P_{24}$ and $P_{25}$) subpeaks, respectively (red lines). In ABA-FLG (blue lines), LO + ZO' consists of one asymmetrical peak centered at ~1745 cm$^{-1}$ (referred here as $P_1$) and the peak energy increases with $N_G$ (up to 5L). These results are in excellent agreement with those reported for exfoliated ABA and ABC-FLG [58,59] and conclusively identify our domains with different FWHM(2D) (see Fig. 2(b) and Fig. S4 in supporting information) as ABA and ABC-FLG. Details on the methodology used to identify ABA and ABC domains in our work are reported in Section 6 of the supporting information.

The ABA- and ABC- FLG show a negligible D peak intensity (ratio of the intensities of D and G band, $I_D/I_G = 0$–$6.5 \times 10^{-3}$), which indicates a good crystalline quality of the FLG (See Fig. S2 in supporting information) [60].

Since Raman measurements are limited in terms of spatial resolution by the size of the laser spot (~1 μm), we used scattering-type scanning near-field microscopy (s-SNOM) [61,62] to further analyze the FLG crystals. In such measurements, the spatial resolution is determined by the tip radius, in our case 20–30 nm. Additionally, the technique allows to acquire local topographic and optical conductivity information simultaneously. A s-SNOM topography image of a portion of crystal F2 (yellow square in Fig. 2(b)) is displayed in Fig. 3(a), showing a FLG with varying thickness (4L–6L). The FWHM(2D) Raman map over the same FLG area of Fig. 3(a) is shown in Fig. 3(b) (The map is extracted from area indicated with a yellow square in Fig. 2(b) and aligned with respect
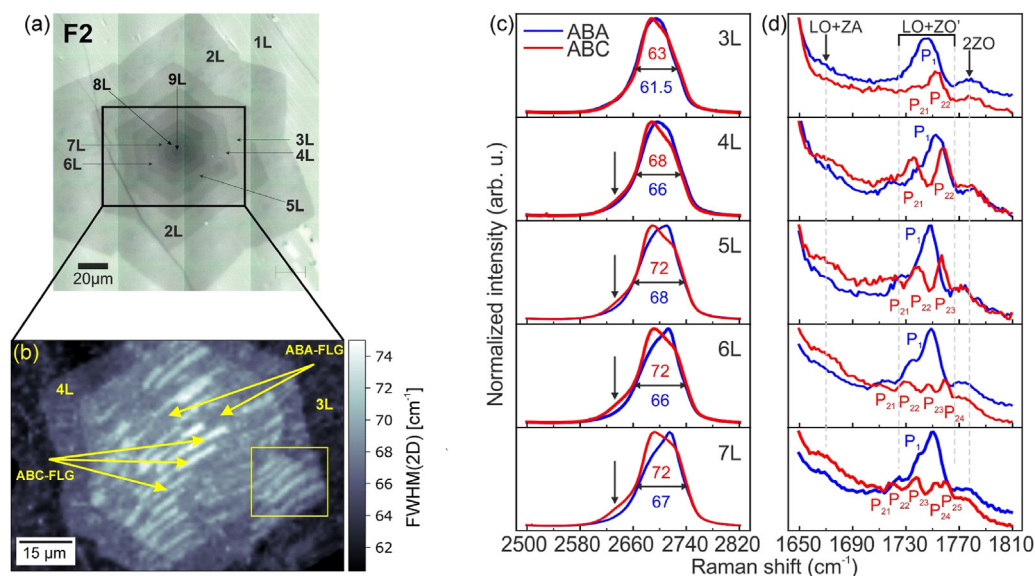


**Fig. 2.** a) BF-OM of FLG crystal F2. $N_G$ is indicated and up to 9L can be appreciated. b) FWHM(2D) Raman map, on 3L–9L FLG area (black rectangle in a); step size is 1 μm. The ABA- and ABC-stacked FLG are indicated. c) 2D band for ABA-stacked (blue) and ABC-stacked (red) FLG, from 3L to 7L. The values of FWHM(2D) are reported and the arrows indicate the enhanced shoulder peak characteristic of ABC-FLG. d) M band for ABA-stacked (blue) and ABC-stacked (red) FLG, from 3L to 7L. The individual components of the M band are indicated. (A colour version of this figure can be viewed online.)
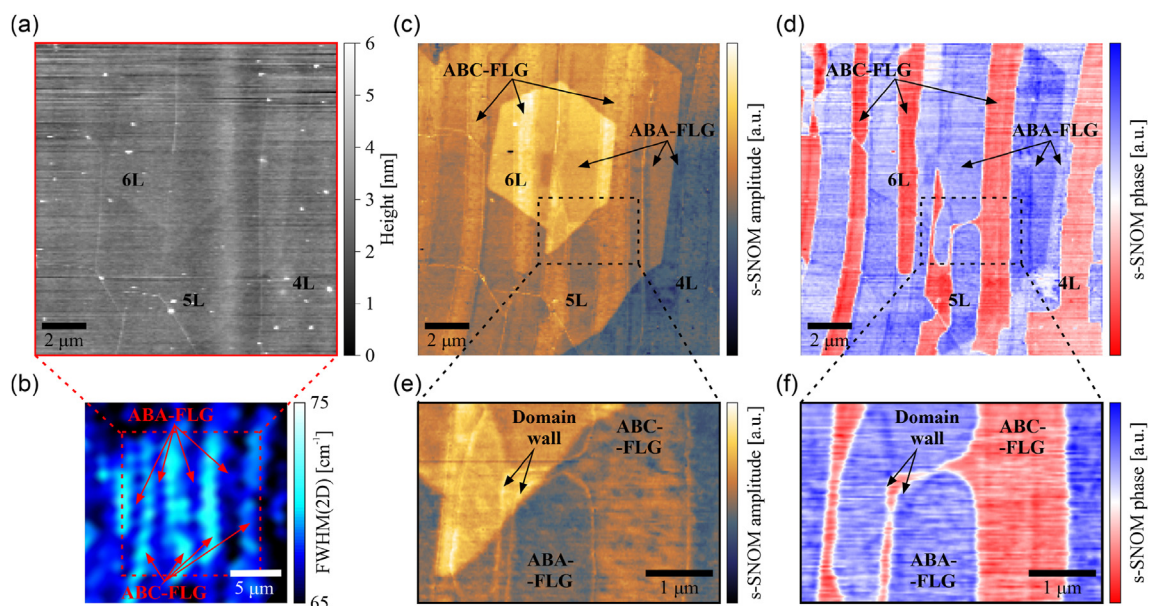
**Fig. 3.** a) Topography image of the region marked by the yellow rectangle in Fig. 2(b). b) FWHM(2D) Raman map of the same region shown in a). The map is aligned with the crystal orientation in a). c) and d) s-SNOM amplitude and phase of the same region shown in (a), respectively. e) and f) high-resolution s-SNOM amplitude and phase images of the regions indicated rectangle in (b) and (c), respectively. (A colour version of this figure can be viewed online.)

to the crystal orientation in Fig. 3(a)). While the topographic image does not show the stripe-like domains of different stacking identified in the Raman map (Fig. 3(b)), vertically oriented domains with different stacking are clearly seen in the s-SNOM amplitude and phase shown in Fig. 3(c) and (d) [27,45,46]. The amplitude signal increases with increasing layer number [27,46], while the phase signal is more sensitive to stacking order. The distribution of the domains obtained by s-SNOM matches perfectly with the Raman observations, thus confirming the width of the stripes of alternating stacking order (micron scale) and their lengths (tens of microns). Surprisingly, the ABA and ABC stripes are not perturbed by changes in the layer number, i.e. the stacking is conserved across atomic steps. This is a clear indication, that the stacking order is not dependent on the layer number. A further indication that other factors than layer number determine the stacking comes from the observation that the stripes of the same stacking order follow the folds visible in the topography (see below for a discussion on the mechanism of how the changes in stacking order emerge). Finally, we have performed high-resolution scans, shown in Fig. 3 (e) and (f), which clearly show that the individual stacking domains are single crystalline (i.e. without further local stacking changes) on the micron scale. However, in a few cases we observed domain walls corresponding to stacking transformation *across* the stripes, as exemplified by the ABC patch interrupting the ABA region in Fig. 3(e) and (f).

The distribution of the ABA and ABC domains in our FLG crystals resembles the SB pattern developed by Cu upon graphene growth (appreciable in DF-OM Fig. 1(e)). Indeed, when comparing BF-OM images of the Cu substrate after the transfer of FLG with the FWHM(2D) Raman maps of the same FLG crystals on $SiO_2$/Si, the origin of the ABC stripes appears to be bounded to the Cu substrate morphology. As visible in Fig. 4(a) and Fig. S8 in supporting information, after graphene transfer, the crystals' hexagonal shape remains imprinted on the Cu foil. The SB associated with different $N_G$ (i.e. increasing step height for increasing $N_G$) is also clearly visible, allowing one to resolve the growth regions for different FLG thickness. To illustrate the strong correlation between the Cu steps and the domains with different stacking orders, in Fig. 4(b) we

show a superposition of a BF-OM image of the leftover Cu and a Raman FWHM(2D) map of FLG crystal F3 after the transfer (the same is done for F2 and F4 in Fig. S8 in supporting information). The similarity between the shape of the stripe-like domains with alternating stacking and the Cu substrate is compelling. The ABA (black-color) and ABC (white-color) regions follow exactly the Cu steps on the growth substrate. In addition, in Fig. 4(c), we show a spatial profile of FWHM(2D) in the 4L region of F3, together with the position of the $P_1$ and $P_{22}$ peaks, which allow for visualizing the alternation between ABC and ABA stripes across the Cu steps (see section 6 and Fig. S6 in supporting information for more details). For ABC-FLG, the higher frequency subpeaks ($P_{22}$ in this case) are blueshifted with respect to the main peak $P_1$ of ABA-FLG. Thus, the line scan of the position of $P_1$ and $P_{22}$ can be used to track the distribution of the ABA and ABC domains and corroborate the oscillating behavior of FWHM(2D).

Fig. 4(d) shows a topographic AFM image of FLG crystal F1 on Cu substrate, taken over a 3L–8L region. An additional AFM topography image over 1L–2L areas is shown in Fig. S9 in supporting information. Fig. 3(e) shows the height profile along the blue line in Fig. 3(d). The FLG/Cu surface has a clear terrace-step like structure. Underneath FLG, the Cu surface morphology changes dramatically. Two parallel alternating regions with different structures and roughness become distinguishable. As shown in Fig. 4(d) and (e), the first region (dubbed α) is composed of one large terrace-step, with a step height of about 80–100 nm and with terrace width of 1–2 μm. The other region (dubbed β) is composed of high-density terraces-steps, with ~400 nm wide terraces with step height ~40 nm. By comparing Fig. 4(e) and (c), one observes that the FLG/Cu corrugations closely resemble the spatial correlation of the Raman parameters in FLG, with the ABA/ABC boundaries corresponding to transitions between α and β type SB. SEM analysis also confirms the presence of alpha and beta regions on the Cu substrate after graphene detachment (see Fig. S10 in supporting information).

Having established the correlation between alternating ABA/ABC stripes in CVD-grown FLG and the surface of the Cu catalyst, we now address the mechanisms that underlie the stabilization of the
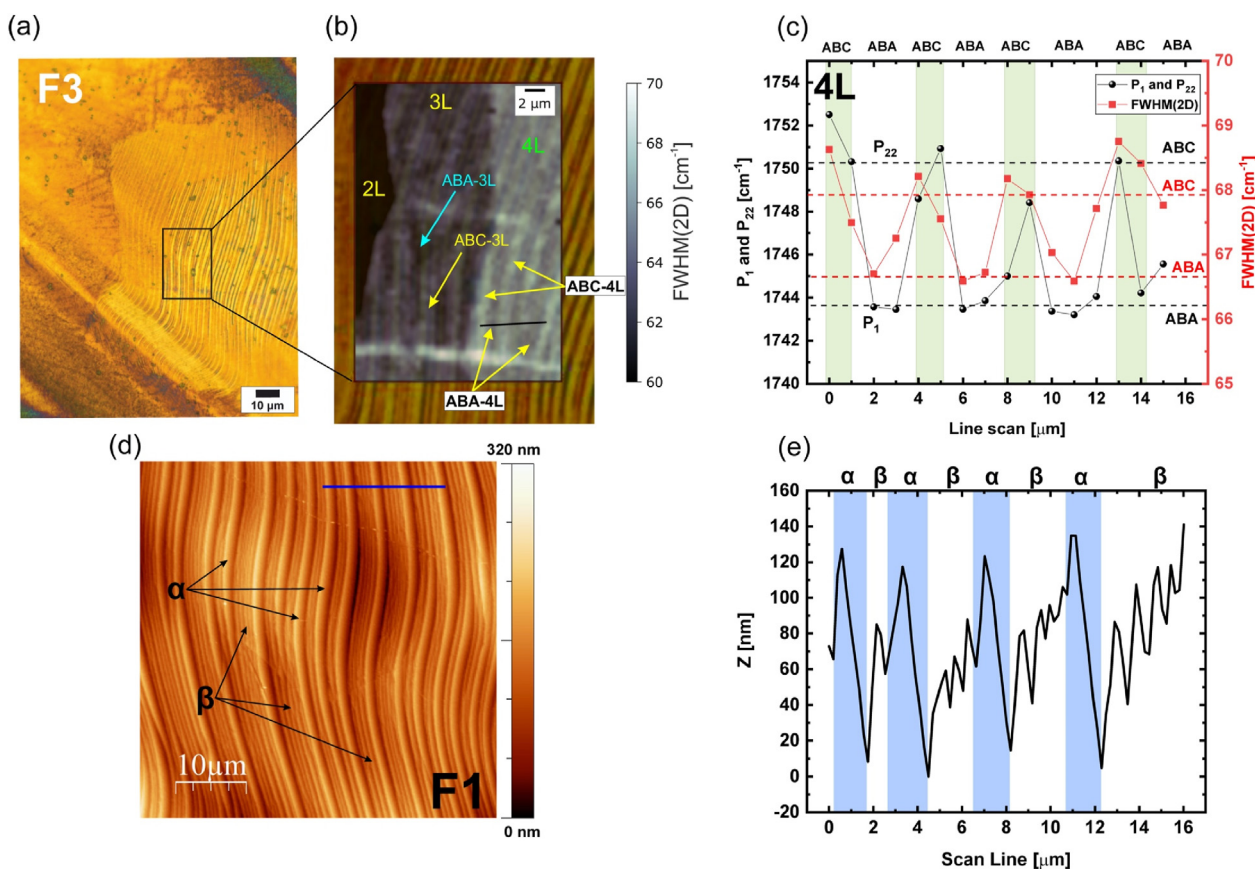
**Fig. 4.** a) BF-OM of the Cu substrate after detachment of FLG crystal F3. b) Superposition of a) with the FWHM(2D) Raman mapping of the transferred FLG F3. c) Spatial correlation of FWHM(2D) and position of peaks $P_1$ and $P_{22}$, taken along the black line in b), with dashed lines as a guide to the eye. d) AFM image of FLG F1 (3L—8L thick) on Cu. e) AFM height profile taken along the blue line in d). The x scale matches the one used in c). (A colour version of this figure can be viewed online.)

ABC-stacked domains. Gao et al. [37] have recently highlighted the central role of the substrate-FLG interaction and pointed out that the formation of ABC-FLG is promoted by the substrate curvature. Despite some similarities with our results, we note that, apart from obtaining smaller and thinner (mostly 3L and up to 5L) ABC domains, in Ref. [37] a different catalyst (Cu/Ni alloy), displaying considerable differences in the SB morphology, was used. Therefore, we shall consider several factors specific to our synthesis process.

SB on Cu can be attributed to either strain relaxation during the cool-down step [49,63,64] or minimization of the bending energy of FLG during the growth step [37,50], which supports increased-height SB when Cu is covered by thick FLG, as we observe experimentally. Han et al. [65] have recently shown that the bending rigidity of FLG strongly depends on its curvature, reporting considerable softening at large bending angles (>40°). Importantly, this soft regime relies on the slipping of atomic planes within FLG, which is proposed as a mechanism stabilizing ABC-FLG [66], as well as governing FLG stacking transformation under shear stress [21]. We tentatively attribute the formation of ABA/ABC domain walls to interlayer displacements at large bending angle of FLG at the α/β SB boundaries. However, according to Refs. [21,66], the direction of interlayer slipping with respect to the FLG crystallographic orientation is crucial in stabilizing ABC-FLG. Therefore, we shall consider *(i)* the crystallographic orientation of the hexagonal-shaped FLG and *(ii)* how the ABC stripes distribute along the Cu steps.

In Fig. 5(a), we show a 25 μm field of view (FOV) LEEM micrograph of FLG crystal F5 with thickness up to 4L, after semi-dry transfer to ZLG/SiC substrate. Fig. 5(b) shows the corresponding

reciprocal space LEED, which allows identifying the crystallographic directions of FLG. The FLG hexagons are zigzag (ZZ) terminated, as preferentially found for isolated graphene crystals on Cu [67]. An evenly spaced series of aligned wrinkles is visible approximately along the armchair (AC) direction. These features are imprinted from the Cu morphology and likely indicate the main docking orientation of the crystal along the Cu steps, which is known to be isoenergetic for ZZ and AC edges [68] (see Fig. S11 for more information about the morphology of FLG and the wrinkles originating from the corrugated structure of FLG/Cu).

The Cu steps under FLG, as we have shown by different imaging techniques both before and after transfer of FLG, have a characteristic wavy morphology (see Fig. 4(d) and Figs. S8 and S10 in supporting information). This implies that bending of FLG and, consequently, interlayer slipping takes place along different directions, determined by the wavy SB pattern. As illustrated in the simple sketch of Fig. 5(d), interlayer displacement along the ZZ direction does not perturb ABA-FLG, while along the AC direction it can drive a stacking transformation to ABC.

Indeed, Nery et al. [66] have proposed a strongly orientation-dependent stability diagram for ABC-FLG, which preferentially form under shear-and-slip along AC. We can test this scenario by analyzing a Raman FWHM(2D) map of this specific FLG crystal (F5), as shown in Fig. 5(c). No ABC domains are found in the left portion of FLG, where wrinkles (derived from Cu steps) are aligned to AC (i.e. the layers displace along ZZ). In contrast, the right part shows numerous ABC stripes, corresponding to in-plane orientation of the Cu steps toward ZZ (interlayer displacement along AC). Assuming ZZ termination for the hexagonal crystals [67], we can investigate
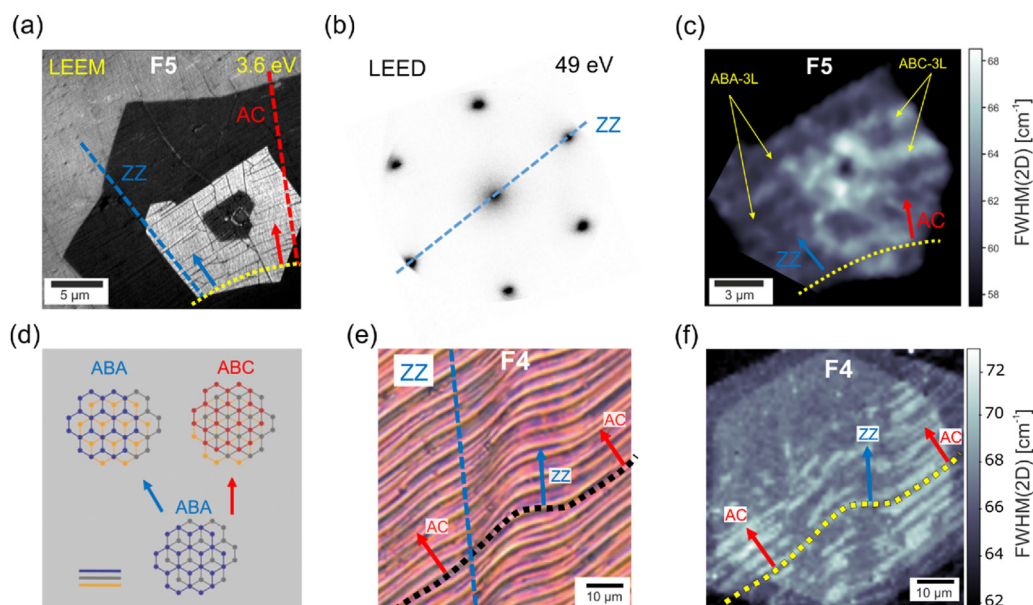
**Fig. 5.** a) LEEM real space image of FLG crystal F5 transferred on ZLG/SiC, recorded at 3.6 eV on a 25 μm FOV. The yellow dotted line traces the imprinted Cu terraces, the blue and red arrows indicate the direction perpendicular to the terraces and approximate the ZZ and AC direction, respectively. b) Reciprocal space LEED image of a), recorded at 49 eV. The blue dashed line identifies the ZZ direction in real space. c) FWHM(2D) map of the FLG in panel a). d) Sketch of the formation ABC staking due to interlayer slipping, limited to a 3L unit. Two of the layers (orange and gray) are kept fixed in the AB configuration, the third one (blue) moves along the ZZ (blue) or AC (red) direction. Similar diagrams are proposed in Ref. [21]. e) BF-OM of Cu foil after detachment of FLG crystal F4. The Cu steps and the slip orientation are indicated as in panel a). f) FWHM(2D) over the FLG isolated from the portion of the foil in e) and transferred to SiO$_2$. (A colour version of this figure can be viewed online.)

this mechanism also in other FLG samples. In Fig. 5(e) and (f) and Fig. S12 in supporting information, we show that the presence of ABC stripes is tied to the local orientation of the wavy Cu steps with respect to the ZZ and AC crystallographic directions. Similarly, to the height of the steps, their degree of "waviness" seems depending on N$_G$ rather than being an intrinsic feature of the Cu foil. Our observations suggest a strongly coupled evolution of the FLG/Cu system during growth, which involves and controls the stacking order of FLG.

## 4. Conclusions

In this work, we introduce a novel approach to the CVD growth of large area FLG crystals, which can yield thicknesses N$_G$ of 9L or more. Those crystals exhibit alternating stripes with ABA and ABC stacking. ABC-FLG domains show unambiguous Raman fingerprints and extend over device-compatible areas (few tens micrometers long and few micrometers large). The single-crystallinity of the stripe-like domains on a micron scale with alternating stacking order and the independence of stacking order with layer number is confirmed with near-field microscopy. Using different experimental techniques, we reveal a strong correlation between the Cu surface morphology after CVD and the formation of ABA/ABC stripes. Our observations can be explained by stabilization of rhombohedral stacking via directional shear-and-slip across boundaries between different SB features on the Cu surface. The synthesis and transfer of ABC-stacked FLG demonstrated in this work, as well as the understanding of its origin and stabilization, are instrumental towards the achievement of large-scale rhombohedral graphene for applications.

## Data availability

The data that support the findings of this study are available from the corresponding author upon reasonable request.

## CRediT authorship contribution statement

**Chamseddine Bouhafs:** Investigation, Conceptualization, Visualization, Validation, Formal analysis, Methodology, Writing — original draft. **Sergio Pezzini:** Investigation, Methodology, Writing — review & editing. **Fabian R. Geisenhof:** Investigation, Methodology, Visualization, Validation, Formal analysis, Writing — review & editing. **Neeraj Mishra:** Investigation, Writing — review & editing. **Vaidotas Mišeikis:** Investigation, Resources, Writing — review & editing. **Yuran Niu:** Investigation, Writing — review & editing. **Claudia Struzzi:** Investigation, Writing — review & editing. **R. Thomas Weitz:** Investigation, Methodology, Visualization, Validation, Formal analysis, Writing — review & editing. **Alexei A. Zakharov:** Investigation, Resources, Writing — review & editing. **Stiven Forti:** Investigation, Conceptualization, Visualization, Validation, Methodology, Writing — review & editing. **Camilla Coletti:** Investigation, Conceptualization, Visualization, Validation, Methodology, Resources, Writing — review & editing, Supervision, Project administration, Funding acquisition.

## Declaration of competing interest

The authors declare that they have no known competing financial interests or personal relationships that could have appeared to influence the work reported in this paper.

## Acknowledgement

## Appendix A. Supplementary data

Supplementary data to this article can be found online at https://doi.org/10.1016/j.carbon.2021.02.082.

## References

[1] P. Ajayan, P. Kim, K. Banerjee, Two-dimensional van der Waals materials, Phys. Today 69 (2016) 38—44, https://doi.org/10.1063/PT.3.3297.

[2] J.D. Bernal, W.L. Bragg, The structure of graphite, Proc. R. Soc. Lond. - Ser. A Contain. Pap. a Math. Phys. Character 106 (1924) 749—773, https://doi.org/10.1098/rspa.1924.0101.

[3] H.S. Lipson, A.R. Stokes, W.L. Bragg, The structure of graphite, Proc. R. Soc. London. Ser. A. Math. Phys. Sci. 181 (1942) 101—105, https://doi.org/10.1098/rspa.1942.0063.

[4] M.F. Craciun, S. Russo, M. Yamamoto, J.B. Oostinga, A.F. Morpurgo, S. Tarucha, Trilayer graphene is a semimetal with a gate-tunable band overlap, Nat. Nanotechnol. 4 (2009) 383—388, https://doi.org/10.1038/nnano.2009.89.

[5] E.A. Henriksen, D. Nandi, J.P. Eisenstein, Quantum Hall effect and semimetallic behavior of dual-gated ABA-stacked trilayer graphene, Phys. Rev. X. 2 (2012) 11004, https://doi.org/10.1103/PhysRevX.2.011004.

[6] M. Aoki, H. Amawashi, Dependence of band structures on stacking and field in layered graphene, Solid State Commun. 142 (2007) 123—127, https://doi.org/10.1016/j.ssc.2007.02.013.

[7] C.H. Lui, Z. Li, K.F. Mak, E. Cappelluti, T.F. Heinz, Observation of an electrically tunable band gap in trilayer graphene, Nat. Phys. 7 (2011) 944—947, https://doi.org/10.1038/nphys2102.

[8] W. Bao, L. Jing, J. Velasco, Y. Lee, G. Liu, D. Tran, B. Standley, M. Aykol, S.B. Cronin, D. Smirnov, M. Koshino, E. McCann, M. Bockrath, C.N. Lau, Stacking-dependent band gap and quantum transport in trilayer graphene, Nat. Phys. 7 (2011) 948—952, https://doi.org/10.1038/nphys2103.

[9] A.A. Burkov, M.D. Hook, L. Balents, Topological nodal semimetals, Phys. Rev. B 84 (2011) 235126, https://doi.org/10.1103/PhysRevB.84.235126.

[10] C.-H. Ho, C.-P. Chang, M.-F. Lin, Evolution and dimensional crossover from the bulk subbands in ABC-stacked graphene to a three-dimensional Dirac cone structure in rhombohedral graphite, Phys. Rev. B 93 (2016) 75437, https://doi.org/10.1103/PhysRevB.93.075437.

[11] N.B. Kopnin, T.T. Heikkilä, G.E. Volovik, High-temperature surface superconductivity in topological flat-band systems, Phys. Rev. B 83 (2011) 220503, https://doi.org/10.1103/PhysRevB.83.220503.

[12] D. Pierucci, H. Sediri, M. Hajlaoui, J.-C. Girard, T. Brumme, M. Calandra, E. Velez-Fort, G. Patriarche, M.G. Silly, G. Ferro, V. Soulière, M. Marangolo, F. Sirotti, F. Mauri, A. Ouerghi, Evidence for flat bands near the fermi level in epitaxial rhombohedral multilayer graphene, ACS Nano 9 (2015) 5432—5439, https://doi.org/10.1021/acsnano.5b01239.

[13] H. Henck, J. Avila, Z. Ben Aziza, D. Pierucci, J. Baima, B. Pamuk, J. Chaste, D. Utt, M. Bartos, K. Nogajewski, B.A. Piot, M. Orlita, M. Potemski, M. Calandra, M.C. Asensio, F. Mauri, C. Faugeras, A. Ouerghi, Flat electronic bands in long sequences of rhombohedral-stacked graphene, Phys. Rev. B 97 (2018) 245421, https://doi.org/10.1103/PhysRevB.97.245421.

[14] T.T. Heikkilä, G.E. Volovik, in: P.D. Esquinazi (Ed.), Flat Bands as a Route to High-Temperature Superconductivity in Graphite BT - Basic Physics of Functionalized Graphite, Springer International Publishing, Cham, 2016, pp. 123—143, https://doi.org/10.1007/978-3-319-39355-1_6.

[15] T. Scheike, W. Böhlmann, P. Esquinazi, J. Barzola-Quiquia, A. Ballestar, A. Setzer, Can doping graphite trigger room temperature superconductivity? Evidence for granular high-temperature superconductivity in water-treated graphite powder, Adv. Mater. 24 (2012) 5826—5831, https://doi.org/10.1002/adma.201202219.

[16] R. Olsen, R. van Gelderen, C.M. Smith, Ferromagnetism in ABC-stacked trilayer graphene, Phys. Rev. B 87 (2013) 115414, https://doi.org/10.1103/PhysRevB.87.115414.

[17] Y. Lee, S. Che, J.V. Jr, D. Tran, J. Baima, F. Mauri, M. Calandra, M. Bockrath, C.N. Lau, Gate Tunable Magnetism and Giant Magnetoresistance in ABC-Stacked Few-Layer Graphene, arXiv:1911.04450.

[18] Y. Shi, S. Xu, Y. Yang, S. Slizovskiy, S. V Morozov, S.-K. Son, S. Ozdemir, C. Mullan, J. Barrier, J. Yin, A.I. Berdyugin, B.A. Piot, T. Taniguchi, K. Watanabe, V.I. Fal'ko, K.S. Novoselov, A.K. Geim, A. Mishchenko, Electronic phase separation in multilayer rhombohedral graphite, Nature 584 (2020) 210—214, https://doi.org/10.1038/s41586-020-2568-2.

[19] B. Pamuk, J. Baima, F. Mauri, M. Calandra, Magnetic gap opening in rhombohedral-stacked multilayer graphene from first principles, Phys. Rev. B 95 (2017) 75422, https://doi.org/10.1103/PhysRevB.95.075422.

[20] J. Baima, F. Mauri, M. Calandra, Field-effect-driven half-metallic multilayer graphene, Phys. Rev. B 98 (2018) 75418, https://doi.org/10.1103/PhysRevB.98.075418.

[21] Y. Yang, Y.-C. Zou, C.R. Woods, Y. Shi, J. Yin, S. Xu, S. Ozdemir, T. Taniguchi, K. Watanabe, A.K. Geim, K.S. Novoselov, S.J. Haigh, A. Mishchenko, Stacking order in graphite films controlled by van der Waals technology, Nano Lett. 19 (2019) 8526—8532, https://doi.org/10.1021/acs.nanolett.9b03014.

[22] C.H. Lui, Z. Li, Z. Chen, P. V Klimov, L.E. Brus, T.F. Heinz, Imaging stacking order in few-layer graphene, Nano Lett. 11 (2011) 164—169, https://doi.org/10.1021/nl1032827.

[23] C. Coletti, S. Forti, A. Principi, K. V Emtsev, A.A. Zakharov, K.M. Daniels, B.K. Daas, M.V.S. Chandrashekhar, T. Ouisse, D. Chaussende, A.H. MacDonald, M. Polini, U. Starke, Revealing the electronic band structure of trilayer graphene on SiC: an angle-resolved photoemission study, Phys. Rev. B 88 (2013) 155439, https://doi.org/10.1103/PhysRevB.88.155439.

[24] W. Wang, Y. Shi, A.A. Zakharov, M. Syväjärvi, R. Yakimova, R.I.G. Uhrberg, J. Sun, Flat-band electronic structure and interlayer spacing influence in rhombohedral four-layer graphene, Nano Lett. 18 (2018) 5862—5866, https://doi.org/10.1021/acs.nanolett.8b02530.

[25] K. Sugawara, N. Yamamura, K. Matsuda, W. Norimatsu, M. Kusunoki, T. Sato, T. Takahashi, Selective fabrication of free-standing ABA and ABC trilayer graphene with/without Dirac-cone energy bands, NPG Asia Mater. 10 (2018), https://doi.org/10.1038/am.2017.238 e466—e466.

[26] T. Latychevskaia, S.-K. Son, Y. Yang, D. Chancellor, M. Brown, S. Ozdemir, I. Madan, G. Berruto, F. Carbone, A. Mishchenko, K.S. Novoselov, Stacking transition in rhombohedral graphite, Front. Physiol. 14 (2018) 13608, https://doi.org/10.1007/s11467-018-0867-y.

[27] F.R. Geisenhof, F. Winterer, S. Wakolbinger, T.D. Gokus, Y.C. Durmaz, D. Priesack, J. Lenz, F. Keilmann, K. Watanabe, T. Taniguchi, R. Guerrero-Avilés, M. Pelc, A. Ayuela, R.T. Weitz, Anisotropic strain-induced soliton movement changes stacking order and band structure of graphene multilayers: implications for charge transport, ACS Appl. Nano Mater. 2 (2019) 6067—6075, https://doi.org/10.1021/acsanm.9b01603.

[28] J. Zhang, J. Han, G. Peng, X. Yang, X. Yuan, Y. Li, J. Chen, W. Xu, K. Liu, Z. Zhu, W. Cao, Z. Han, J. Dai, M. Zhu, S. Qin, K.S. Novoselov, Light-induced irreversible structural phase transition in trilayer graphene, Light Sci. Appl. 9 (2020) 174, https://doi.org/10.1038/s41377-020-00412-6.

[29] H. Li, M.I.B. Utama, S. Wang, W. Zhao, S. Zhao, X. Xiao, Y. Jiang, L. Jiang, T. Taniguchi, K. Watanabe, A. Weber-Bargioni, A. Zettl, F. Wang, Global control of stacking-order phase transition by doping and electric field in few-layer graphene, Nano Lett. 20 (2020) 3106—3112, https://doi.org/10.1021/acs.nanolett.9b05092.

[30] V. Miseikis, D. Convertino, N. Mishra, M. Gemmi, T. Mashoff, S. Heun, N. Haghighian, F. Bisio, M. Canepa, V. Piazza, C. Coletti, Rapid CVD growth of millimetre-sized single crystal graphene using a cold-wall reactor, 2D Mater. 2 (2015) 14006, https://doi.org/10.1088/2053-1583/2/1/014006.

[31] Y. Hao, L. Wang, Y. Liu, H. Chen, X. Wang, C. Tan, S. Nie, J.W. Suk, T. Jiang, T. Liang, J. Xiao, W. Ye, C.R. Dean, B.I. Yakobson, K.F. McCarty, P. Kim, J. Hone, L. Colombo, R.S. Ruoff, Oxygen-activated growth and bandgap tunability of large single-crystal bilayer graphene, Nat. Nanotechnol. 11 (2016) 426—431, https://doi.org/10.1038/nnano.2015.322.

[32] X. Li, C.W. Magnuson, A. Venugopal, R.M. Tromp, J.B. Hannon, E.M. Vogel, L. Colombo, R.S. Ruoff, Large-area graphene single crystals grown by low-pressure chemical vapor deposition of methane on copper, J. Am. Chem. Soc. 133 (2011) 2816—2819, https://doi.org/10.1021/ja109793s.

[33] Y. Hao, M.S. Bharathi, L. Wang, Y. Liu, H. Chen, S. Nie, X. Wang, H. Chou, C. Tan, B. Fallahazad, H. Ramanarayan, C.W. Magnuson, E. Tutuc, B.I. Yakobson, K.F. McCarty, Y.-W. Zhang, P. Kim, J. Hone, L. Colombo, R.S. Ruoff, The role of surface oxygen in the growth of large single-crystal graphene on copper, Science 342 (2013) 720—723, https://doi.org/10.1126/science.1243879.

[34] X. Li, W. Cai, J. An, S. Kim, J. Nah, D. Yang, R. Piner, A. Velamakanni, I. Jung, E. Tutuc, S.K. Banerjee, L. Colombo, R.S. Ruoff, Large-area synthesis of high-quality and uniform graphene films on copper foils, Science 324 (2009) 1312—1314, https://doi.org/10.1126/science.1171245.

[35] M. Huang, P. V Bakharev, Z.-J. Wang, M. Biswal, Z. Yang, S. Jin, B. Wang, H.J. Park, Y. Li, D. Qu, Y. Kwon, X. Chen, S.H. Lee, M.-G. Willinger, W.J. Yoo, Z. Lee, R.S. Ruoff, Large-area single-crystal AB-bilayer and ABA-trilayer graphene grown on a Cu/Ni(111) foil, Nat. Nanotechnol. 15 (2020) 289—295, https://doi.org/10.1038/s41565-019-0622-8.

[36] L. Brown, R. Hovden, P. Huang, M. Wojcik, D.A. Muller, J. Park, Twinning and twisting of tri- and bilayer graphene, Nano Lett. 12 (2012) 1609—1615, https://doi.org/10.1021/nl204547v.

[37] Z. Gao, S. Wang, J. Berry, Q. Zhang, J. Gebhardt, W.M. Parkin, J. Avila, H. Yi, C. Chen, S. Hurtado-Parra, M. Drndić, A.M. Rappe, D.J. Srolovitz, J.M. Kikkawa, Z. Luo, M.C. Asensio, F. Wang, A.T.C. Johnson, Large-area epitaxial growth of curvature-stabilized ABC trilayer graphene, Nat. Commun. 11 (2020) 546, https://doi.org/10.1038/s41467-019-14022-3.

[38] M. Saeed, Y. Alshammari, S.A. Majeed, E. Al-Nasrallah, Chemical vapour deposition of graphene—synthesis, characterisation, and applications: a review, Mol 25 (2020), https://doi.org/10.3390/molecules25173856.

[39] K. Jia, H. Ci, J. Zhang, Z. Sun, Z. Ma, Y. Zhu, S. Liu, J. Liu, L. Sun, X. Liu, J. Sun, W. Yin, H. Peng, L. Lin, Z. Liu, Superclean growth of graphene using a cold-wall chemical vapor deposition approach, Angew. Chem. Int. Ed. 59 (2020) 17214—17218, https://doi.org/10.1002/anie.202005406.

[40] N. Lisi, T. Dikonimos, F. Buonocore, M. Pittori, R. Mazzaro, R. Rizzoli, S. Marras, A. Capasso, Contamination-free graphene by chemical vapor deposition in quartz furnaces, Sci. Rep. 7 (2017) 9927, https://doi.org/10.1038/s41598-017-

09811-z.

[41] Y. Wang, Y. Zheng, X. Xu, E. Dubuisson, Q. Bao, J. Lu, K.P. Loh, Electrochemical delamination of CVD-grown graphene film: toward the recyclable use of copper catalyst, ACS Nano 5 (2011) 9927—9933, https://doi.org/10.1021/nn203700w.

[42] V. Miseikis, F. Bianco, J. David, M. Gemmi, V. Pellegrini, M. Romagnoli, C. Coletti, Deterministic patterned growth of high-mobility large-crystal graphene: a path towards wafer scale integration, 2D Mater. 4 (2017) 21004, https://doi.org/10.1088/2053-1583/aa5481.

[43] M.A. Giambra, V. Mišeikis, S. Pezzini, S. Marconi, A. Montanaro, F. Fabbri, V. Sorianello, A.C. Ferrari, C. Coletti, M. Romagnoli, Wafer-scale integration of graphene-based photonic devices, ACS Nano 15 (2021) 3171—3187, https://doi.org/10.1021/acsnano.0c09758.

[44] C. Riedl, C. Coletti, T. Iwasaki, A.A. Zakharov, U. Starke, Quasi-free-Standing epitaxial graphene on SiC obtained by hydrogen intercalation, Phys. Rev. Lett. 103 (2009) 246804, https://doi.org/10.1103/PhysRevLett.103.246804.

[45] L. Ju, Z. Shi, N. Nair, Y. Lv, C. Jin, J. Velasco, C. Ojeda-Aristizabal, H.A. Bechtel, M.C. Martin, A. Zettl, J. Analytis, F. Wang, Topological valley transport at bilayer graphene domain walls, Nature 520 (2015) 650—655, https://doi.org/10.1038/nature14364.

[46] D.-S. Kim, H. Kwon, A.Y. Nikitin, S. Ahn, L. Martín-Moreno, F.J. García-Vidal, S. Ryu, H. Min, Z.H. Kim, Stacking structures of few-layer graphene revealed by phase-sensitive infrared nanoscopy, ACS Nano 9 (2015) 6765—6773, https://doi.org/10.1021/acsnano.5b02813.

[47] S. Forti, S. Link, A. Stöhr, Y. Niu, A.A. Zakharov, C. Coletti, U. Starke, Semi-conductor to metal transition in two-dimensional gold and its van der Waals heterostack with graphene, Nat. Commun. 11 (2020) 2236, https://doi.org/10.1038/s41467-020-15683-1.

[48] X.H. Kong, H.X. Ji, R.D. Piner, H.F. Li, C.W. Magnuson, C. Tan, A. Ismach, H. Chou, R.S. Ruoff, Non-destructive and rapid evaluation of chemical vapor deposition graphene by dark field optical microscopy, Appl. Phys. Lett. 103 (2013) 43119, https://doi.org/10.1063/1.4816752.

[49] J.H. Kang, J. Moon, D.J. Kim, Y. Kim, I. Jo, C. Jeon, J. Lee, B.H. Hong, Strain relaxation of graphene layers by Cu surface roughening, Nano Lett. 16 (2016) 5993—5998, https://doi.org/10.1021/acs.nanolett.6b01578.

[50] D. Yi, D. Luo, Z.-J. Wang, J. Dong, X. Zhang, M.-G. Willinger, R.S. Ruoff, F. Ding, What drives metal-surface step bunching in graphene chemical vapor deposition? Phys. Rev. Lett. 120 (2018) 246101, https://doi.org/10.1103/PhysRevLett.120.246101.

[51] S. Pezzini, V. Mišeikis, S. Pace, F. Rossella, K. Watanabe, T. Taniguchi, C. Coletti, High-quality electrical transport using scalable CVD graphene, 2D Mater. 7 (2020) 41003, https://doi.org/10.1088/2053-1583/aba645.

[52] P. Blake, E.W. Hill, A.H. Castro Neto, K.S. Novoselov, D. Jiang, R. Yang, T.J. Booth, A.K. Geim, Making graphene visible, Appl. Phys. Lett. 91 (2007) 63124, https://doi.org/10.1063/1.2768624.

[53] S. Pezzini, V. Mišeikis, G. Piccinini, S. Forti, S. Pace, R. Engelke, F. Rossella, K. Watanabe, T. Taniguchi, P. Kim, C. Coletti, 30°-Twisted bilayer graphene quasicrystals from chemical vapor deposition, Nano Lett. 20 (2020) 3313—3319, https://doi.org/10.1021/acs.nanolett.0c00172.

[54] L.M. Malard, M.A. Pimenta, G. Dresselhaus, M.S. Dresselhaus, Raman spec-troscopy in graphene, Phys. Rep. 473 (2009) 51—87, https://doi.org/10.1016/j.physrep.2009.02.003.

[55] A.C. Ferrari, J.C. Meyer, V. Scardaci, C. Casiraghi, M. Lazzeri, F. Mauri, S. Piscanec, D. Jiang, K.S. Novoselov, S. Roth, A.K. Geim, Raman spectrum of graphene and graphene layers, Phys. Rev. Lett. 97 (2006) 187401, https://doi.org/10.1103/PhysRevLett.97.187401.

[56] C. Cong, T. Yu, K. Sato, J. Shang, R. Saito, G.F. Dresselhaus, M.S. Dresselhaus, Raman characterization of ABA- and ABC-stacked trilayer graphene, ACS Nano 5 (2011) 8760—8768, https://doi.org/10.1021/nn203472f.

[57] A. Torche, F. Mauri, J.-C. Charlier, M. Calandra, First-principles determination of the Raman fingerprint of rhombohedral graphite, Phys. Rev. Mater. 1 (2017) 41001, https://doi.org/10.1103/PhysRevMaterials.1.041001.

[58] T.A. Nguyen, J.-U. Lee, D. Yoon, H. Cheong, Excitation energy dependent Raman signatures of ABA- and ABC-stacked few-layer graphene, Sci. Rep. 4 (2014) 4630, https://doi.org/10.1038/srep04630.

[59] C.H. Lui, L.M. Malard, S. Kim, G. Lantz, F.E. Laverge, R. Saito, T.F. Heinz, Observation of layer-breathing mode vibrations in few-layer graphene through combination Raman scattering, Nano Lett. 12 (2012) 5539—5544, https://doi.org/10.1021/nl302450s.

[60] L.G. Cançado, A. Jorio, E.H.M. Ferreira, F. Stavale, C.A. Achete, R.B. Capaz, M.V.O. Moutinho, A. Lombardo, T.S. Kulmala, A.C. Ferrari, Quantifying defects in graphene via Raman spectroscopy at different excitation energies, Nano Lett. 11 (2011) 3190—3196, https://doi.org/10.1021/nl201432g.

[61] D. Richards, A. Zayats, F. Keilmann, R. Hillenbrand, Near-field microscopy by elastic light scattering from a tip, in: Philos. Trans. R. Soc. London. Ser. A Math. Phys. Eng. Sci., Royal Society, 2004, pp. 787—805, https://doi.org/10.1098/rsta.2003.1347.

[62] A. V Zayats, D. Richards, Nano-optics and Near-Field Optical Microscopy, Artech House, 2009.

[63] B. Deng, J. Wu, S. Zhang, Y. Qi, L. Zheng, H. Yang, J. Tang, L. Tong, J. Zhang, Z. Liu, H. Peng, Anisotropic strain relaxation of graphene by corrugation on copper crystal surfaces, Small 14 (2018) 1800725, https://doi.org/10.1002/smll.201800725.

[64] J. Tian, H. Cao, W. Wu, Q. Yu, N.P. Guisinger, Y.P. Chen, Graphene induced surface reconstruction of Cu, Nano Lett. 12 (2012) 3893—3899, https://doi.org/10.1021/nl3002974.

[65] E. Han, J. Yu, E. Annevelink, J. Son, D.A. Kang, K. Watanabe, T. Taniguchi, E. Ertekin, P.Y. Huang, A.M. van der Zande, Ultrasoft slip-mediated bending in few-layer graphene, Nat. Mater. 19 (2020) 305—309, https://doi.org/10.1038/s41563-019-0529-7.

[66] J.P. Nery, M. Calandra, F. Mauri, Long-range rhombohedral-stacked graphene through shear, Nano Lett. 20 (2020) 5017—5023, https://doi.org/10.1021/acs.nanolett.0c01146.

[67] Q. Yu, L.A. Jauregui, W. Wu, R. Colby, J. Tian, Z. Su, H. Cao, Z. Liu, D. Pandey, D. Wei, T.F. Chung, P. Peng, N.P. Guisinger, E.A. Stach, J. Bao, S.-S. Pei, Y.P. Chen, Control and characterization of individual grains and grain boundaries in graphene grown by chemical vapour deposition, Nat. Mater. 10 (2011) 443—449, https://doi.org/10.1038/nmat3010.

[68] Z. Yan, Y. Liu, L. Ju, Z. Peng, J. Lin, G. Wang, H. Zhou, C. Xiang, E.L.G. Samuel, C. Kittrell, V.I. Artyukhov, F. Wang, B.I. Yakobson, J.M. Tour, Large hexagonal Bi- and trilayer graphene single crystals with varied interlayer rotations, Angew. Chem. Int. Ed. 53 (2014) 1565—1569, https://doi.org/10.1002/anie.201306317.